

Supplementary Material

Engineering the Ru Nanoparticle Size and Metal-Support Interactions for Enhanced Catalytic Hydrogen Combustion

Zohreh Akbari^{1,2*}, Mohammad Reza Alizadeh Kiapi³, Thi Ha My Pham^{1,2}, Loris Lombardo^{1,2*}, David Fairen-Jimenez³, Andreas Zuttel^{1,2}

¹ Laboratory of Materials for Renewable Energy (LMER), Institute of Chemical Sciences and Engineering (ISIC), Basic Science Faculty (SB), École Polytechnique Fédérale de Lausanne (EPFL) Valais/Wallis, Energypolis, Rue de l'Industrie 17, 1951 Sion, Switzerland

² Empa Materials Science & Technology, 8600 Dübendorf, Switzerland

³ The Adsorption & Advanced Materials Laboratory (A2ML), Department of Chemical Engineering & Biotechnology, University of Cambridge, Philippa Fawcett Drive, Cambridge CB3 0AS, UK

*Zohreh.akbari@epfl.ch

*Loris.Lombardo@epfl.ch

Table of contents:

SI1. H₂-TPR of RuCl₃.xH₂O	3
SI2. Effect of the heat treatment atmosphere on the phase and particle size of Ru catalysts	3
SI3. CHC performance test station	5
SI4. Dispersion of the Ru NPs	6
SI5. The effect of chlorine ions on the CHC activity and H₂ uptake capacity of 1Ru-γAl₂O₃ catalyst	6
SI6. Kinetic data validation using different GHSV	7
SI7. N₂ adsorption/desorption measurements	8
SI8. Details on DFT calculations	8
References	11

SI1. H₂-TPR of RuCl₃.xH₂O

Based on the mass spectrometer signals, the reaction between hydrogen and RuCl₃.xH₂O is:

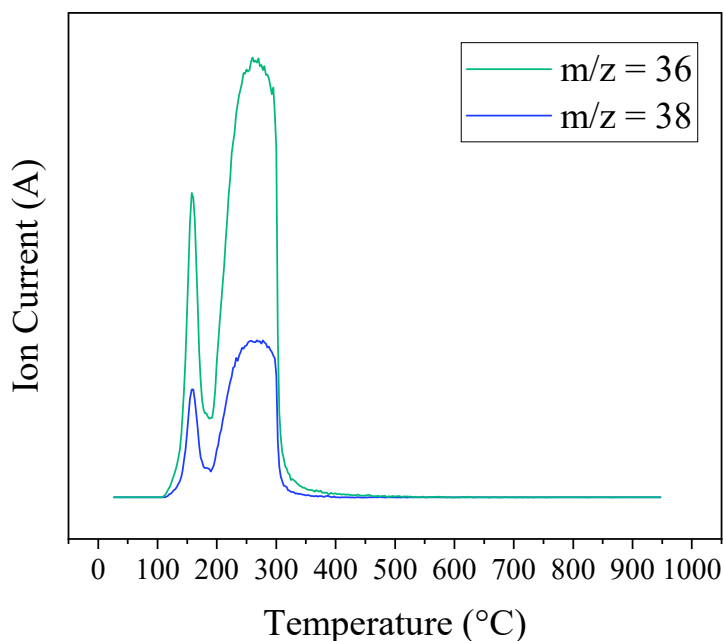
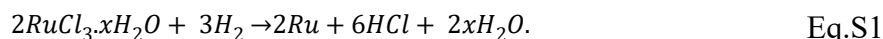


Figure S1. TPR profile of mass to charge (m/z) ratio of 36 and 38. These m/z ratios are the primary mass fractions for HCl, which emerges from RuCl₃.xH₂O decomposition under a reducing atmosphere. The experiment is performed under FG atmosphere from RT to 950 °C with a heating ramp of 5 °C.min⁻¹.

In conjunction with the TPR results of Ru- γ Al₂O₃ catalysts, we used 400°C as the reduction temperature for all Ru- γ Al₂O₃ samples.

SI2. Effect of the heat treatment atmosphere on the phase and particle size of Ru catalysts

The XRD patterns of pure γ Al₂O₃ and 5Ru γ Al₂O₃ catalysts are shown in Figure S2. As can be seen from Figure S2a and b, the support activation does not affect the phase composition of the support. The hydroxide peaks are evident in the as-synthesised catalyst, which vanishes after the subsequent heat treatment (Figure S2c). The heat treatment atmosphere plays a significant

role in the final chemical composition of Ru species. Although the oxidising atmosphere has induced the formation of RuO₂ (Figure S2d), the development of metallic Ru peaks is not observable in Fig. S3e due to the peak overlapping with γ -Al₂O₃ support and the formation of metallic Ru NPs. Further investigation is carried out with STEM to observe the metallic Ru particle presence in the FG heat-treated catalyst.

Furthermore, the chlorine removal step with ammonia solution does not affect the chemical composition of the metallic Ru and support (Figure S2f). Electron microscopy images are presented in Figure S3 for the catalyst calcined under an oxidising atmosphere. Using ImageJ, the average RuO₂ particle size is 22.1 nm, 22 times more than what can be achieved by reducing the catalyst under a reducing atmosphere.

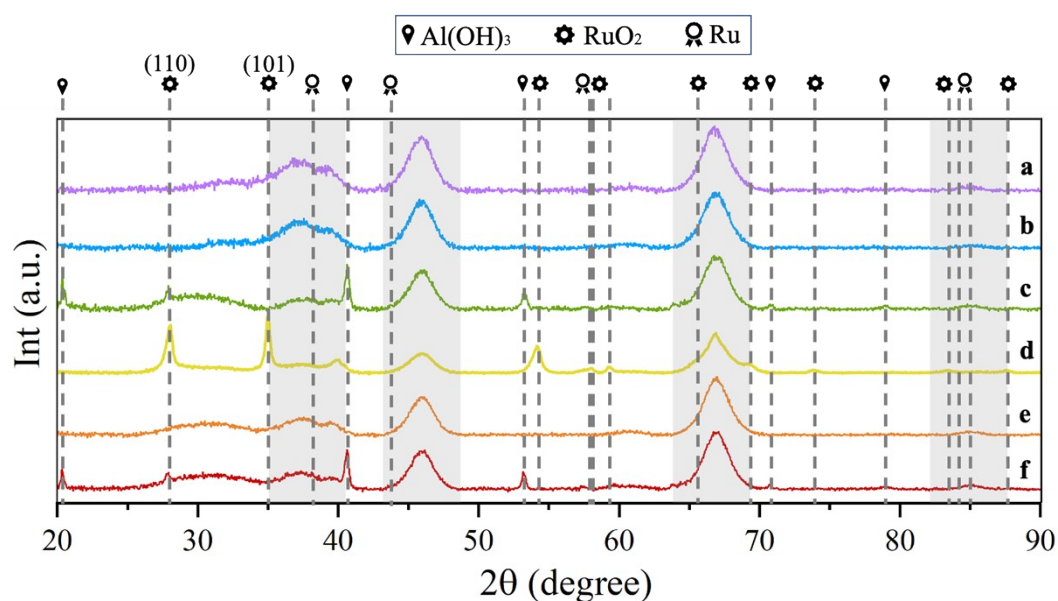


Figure S2. XRD pattern of a) γ -Al₂O₃, b) pre-treated γ -Al₂O₃, c) as-synthesized 5Ru- γ -Al₂O₃, d) 5Ru- γ -Al₂O₃ calcined at 400 °C in air, e) 5Ru- γ -Al₂O₃ calcined at 400 °C in FG and f) 5Ru- γ -Al₂O₃ calcined at 400 °C in FG after Cl removal with an ammonia solution. The grey areas represent the XRD pattern related to pure γ -Al₂O₃.

In summary, the support activation step is assumed to form hydroxyl groups on the support surface. These hydroxyl groups later attract the positively charged Ru ions in the impregnation solution; hence, a highly dispersed xRu- γ -Al₂O₃ is achieved. However, during the calcination step, the oxidising atmosphere leads to Ru atom movement and large RuO₂ agglomerate formation with large particle size distribution and poor dispersity. In contrast, calcination under a reducing atmosphere stabilises the sub-nano-sized Ru NPs.

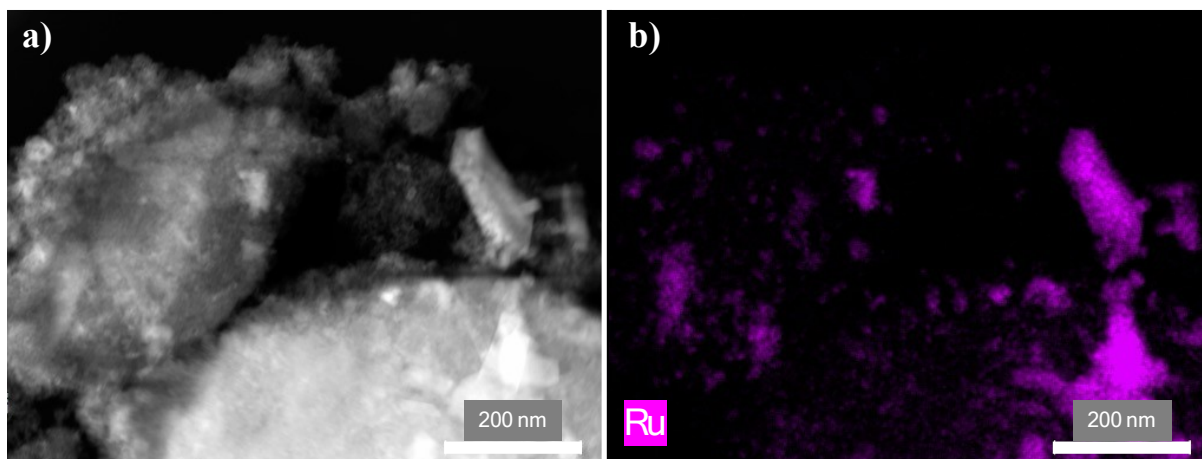


Figure S3. a) HAADF-STEM and b) EDS Ru elemental map of 5Ru- γ Al₂O₃ catalyst calcined in air atmosphere.

SI3. CHC performance test station

Three mass flow controllers (MFCs) feed the gas into a plug-flow microreactor. A capillary tube connected to a mass spectrometer analyses the gas composition.

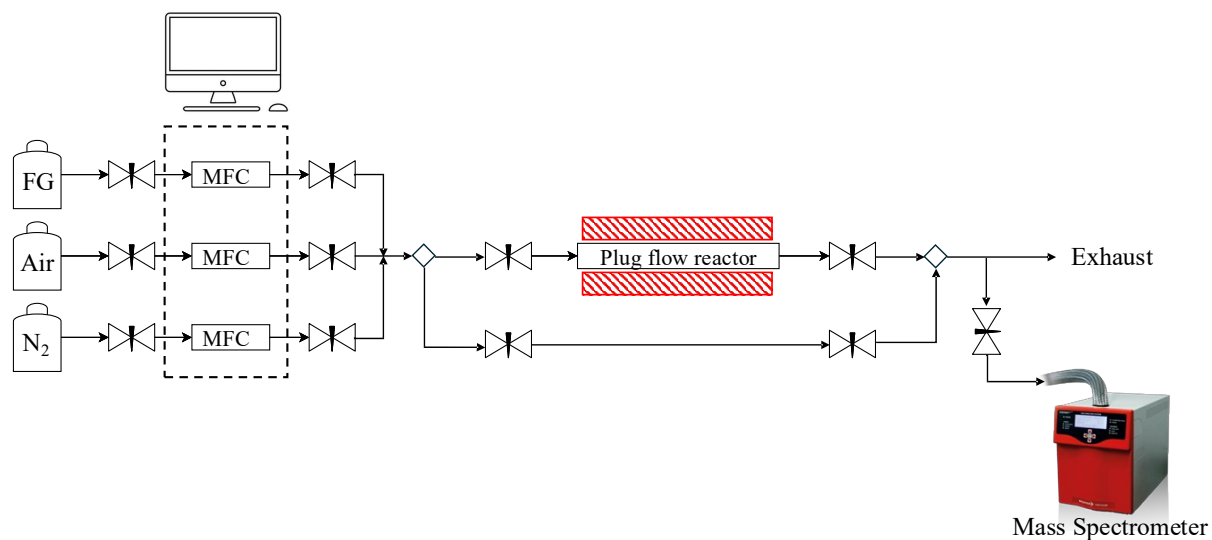


Figure S4. CHC performance test station.

SI4. Dispersion of the Ru NPs

To calculate the Ru NPs' dispersion (D), i.e., the number of surface Ru atoms divided by the total number of Ru atoms in each particle, we have considered Ru NPs as truncated hexagonal bipyramids^{1,2}. The calculated D for different xRu- γ Al₂O₃ catalysts is presented in Table S1.

Table S1. Summary of average particle size and the dispersion of xRu- γ Al₂O₃ catalysts.

	0.5Ru- γ Al ₂ O ₃	1Ru- γ Al ₂ O ₃	2Ru- γ Al ₂ O ₃	5Ru- γ Al ₂ O ₃	10Ru- γ Al ₂ O ₃
Mean particle size (nm)	0.42 ± 0.06	0.75 ± 0.12	1.10 ± 0.11	1.38 ± 0.12	1.60 ± 0.19
Dispersion (%)	97.8	91.2	83.2	76.8	71.8

SI5. The effect of chlorine ions on the CHC activity and H₂ uptake capacity of 1Ru- γ Al₂O₃ catalyst

We were curious about the role of chlorine ions (since the RuCl₃.xH₂O was used as the Ru source) on the activity of the 1Ru- γ Al₂O₃ catalyst. Previous studies have reported divergent observations regarding chlorine ions' poisoning or promotional effect on different reactions over Ru- γ Al₂O₃ catalysts. Mieth et al.³ showed that the residual chlorine ions have a promotional effect on the CO methanation reaction. At the same time, other studies⁴ demonstrated that chlorine ions are poisonous for ammonia synthesis reactions. To the best of our knowledge, no study has provided information on the poisoning or promotional effect of chlorine ions on the CHC reaction. Thus, we performed the CHC reaction over the unwashed and chlorine ions-washed 1Ru- γ Al₂O₃ catalysts (Figure S5a). The findings indicate that chlorine ions have a negative effect on the CHC reaction over the 1Ru- γ Al₂O₃ catalyst. Moreover, H₂ sorption measurements indicate that the presence of chlorine ions decreases the H₂ adsorption capacity in the 1Ru- γ Al₂O₃ catalyst (Figure S5b). The H₂ adsorption capacities are calculated using the BET equation, assuming the formation of a monolayer of adsorbed H₂. Considering the optimum Ru loading to be 1 wt%, the effect of chlorine ion removal on the H₂ uptake capacity is investigated. As shown in Figure S5b, chlorine ion removal increases the H₂ uptake capacity by 42%, from 5.4 to 7.7 cm³.gr⁻¹.

Using XPS measurements, our previous study presented proof of Cl ion removal from a Ru- γ Al₂O₃ catalyst ⁵.

Thus, chloride anions poison the catalyst surface, delaying the start of the reaction and shifting it to higher temperatures. Removing these ions makes more active sites available for the CHC reaction. As such, only chlorine-washed catalysts are investigated in the rest of this study.

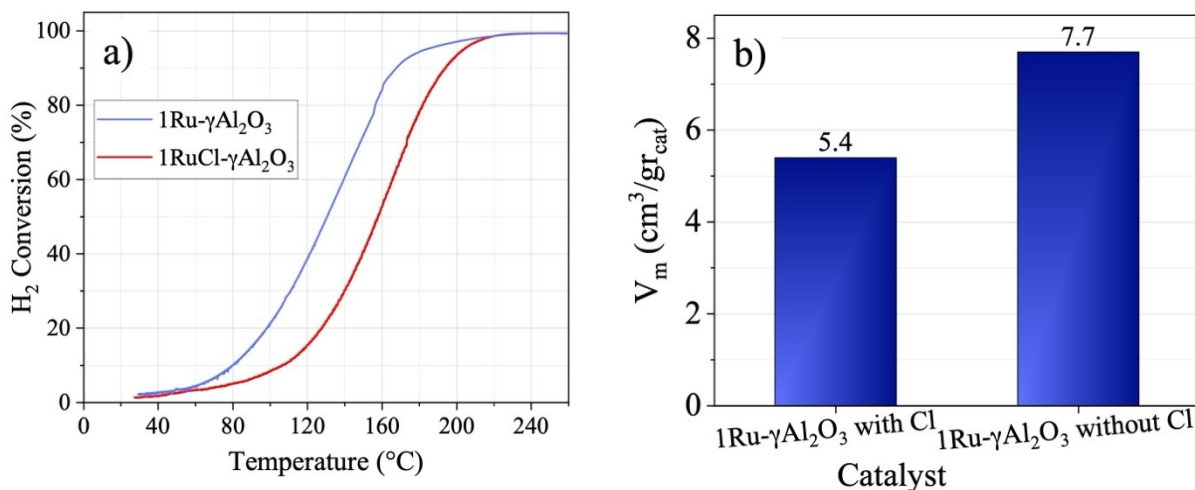


Figure S5. Effect of chlorine ion removal on a) X_{H_2} , and b) H₂ uptake capacity of 1Ru- γ Al₂O₃ catalyst.

SI6. Kinetic data validation using different GHSV

To validate that the kinetic parameters obtained from the experimental data are independent of flow rate, the CHC test is performed on a 2Ru- γ Al₂O₃ catalyst with two different GHSVs, 3000 and 12000 h⁻¹. The obtained E_a values at different GHSVs are reported in Table S2. Therefore, the E_a for 2Ru- γ Al₂O₃ catalyst is 21.8 ± 0.6 kJ.mol⁻¹, with a relative error of 2.86 %.

Table S2. Activation energy variation as a function of GHSV.

GHSV (h ⁻¹)	3000	6000	12000
Activation energy kJ.mol ⁻¹	22.3	22	21.1

SI7. N₂ adsorption/desorption measurements

The samples are degassed at 180 °C for 3.5 h prior to the N₂ adsorption/desorption tests. The Brunauer–Emmett–Teller (BET) method is used to calculate the surface area, and the Barrett–Joyner–Halenda (BJH) method is used to analyse the pore size distribution (Figure S6b).

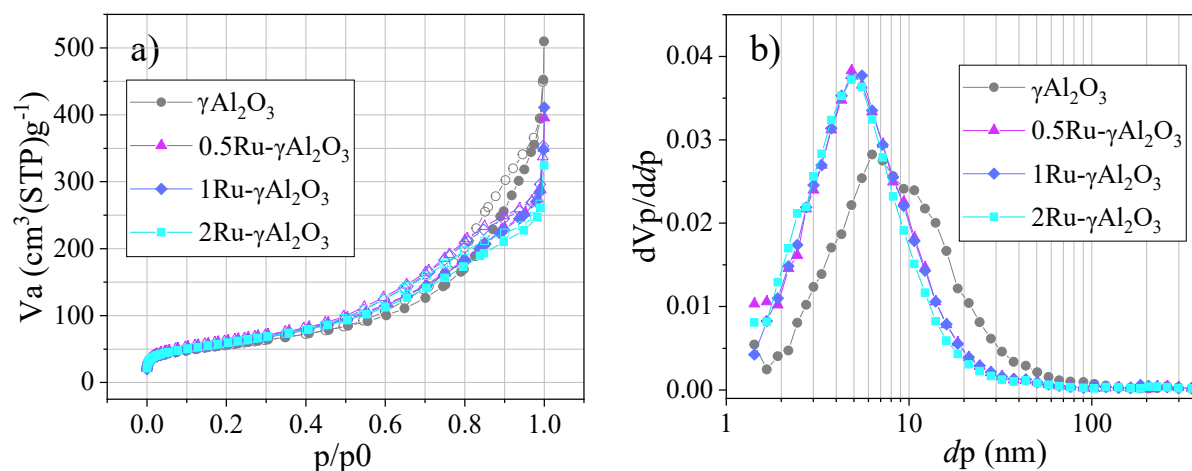


Figure S6. a) N₂ adsorption (solid shapes) and desorption (hollow shapes), and b) pore size distributions of $\gamma\text{Al}_2\text{O}_3$ and xRu- $\gamma\text{Al}_2\text{O}_3$ catalysts.

SI8. Details on DFT calculations

For Gibbs free energy calculations, we followed the workflow outlined in ^{6–8}. The Gibbs free energy for a material can be calculated as:

$$G = E_{DFT} + E_{ZPE} + E_{thermal}(T) - T \times S(T)$$

where E_{DFT} is the total energy directly taken from the single point energy calculation using DFT, E_{ZPE} represents the zero-point energy, T is the temperature in Kelvin, $E_{thermal}(T)$ is the thermal energy contribution at temperature T, and $S(T)$ denotes the entropy at temperature T. E_{ZPE} can be obtained from the vibrational frequency calculated using the density functional perturbation theory (DFPT) method as:

$$E_{ZPE} = \frac{1}{2} \sum h\nu_i$$

where h is the Planck constant, and ν_i is the calculated vibrational frequency of the material. Each of the $E_{thermal}(T)$ and $S(T)$ corrections consist of three terms being vibrational, translational, and rotational terms, which can be shown as:

$$S(T) = S_{vib}(T) + S_r(T) + S_t(T)$$

$$E_{thermal}(T) = E_{thermal,vib}(T) + E_{thermal,r}(T) + E_{thermal,t}(T)$$

For the metal slab as well as the adsorbed atoms, the translational and rotational contributions are negligible and hence, here, only the vibrational effect is considered. In terms of harmonic phonon frequencies ν_i , $E_{thermal,vib}(T)$ can be written as:

$$E_{thermal,vib}(T) = \sum \frac{h\nu_i}{\exp\left(\frac{h\nu_i}{k_B T}\right) - 1}$$

where k_B is the Boltzmann constant. The vibrational entropy can also be calculated from the vibrational frequencies as:

$$S_{vib}(T) = -k_B \sum \ln \left[1 - \exp\left(-\frac{h\nu_i}{k_B T}\right) \right] + \frac{h}{T} \sum \frac{\nu_i}{\exp\left(\frac{h\nu_i}{k_B T}\right) - 1}$$

where k_B is the Boltzmann constant. In the case of gaseous H_2 , O_2 , and H_2O molecules, the rotational and translational thermal and entropy corrections are also included, which can be calculated as:

$$E_{thermal,r} = k_B T$$

$$E_{thermal,t} = \frac{3}{2} k_B T$$

$$S_t = R \left[\ln \left(\left(\frac{2\pi m k_B T}{h^2} \right)^{\frac{3}{2}} \frac{k_B T}{P} \right) + \frac{5}{2} \right]$$

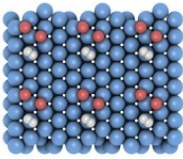
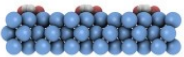
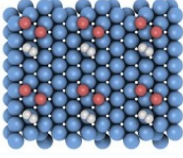
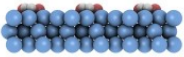
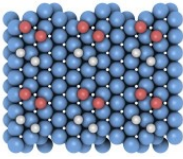
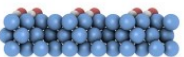
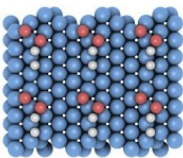
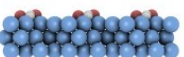
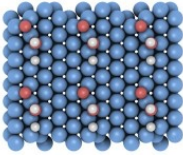
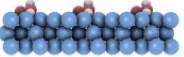
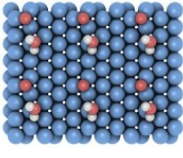
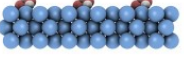
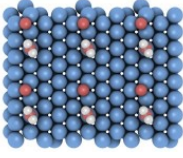
$$S_r = R \left[\frac{1}{2} + \ln \left(\frac{8\pi^2 I k_B T}{\sigma h^2} \right) \right] \text{ (for linear molecules (H}_2 \text{ and O}_2\text{))}$$

$$S_r = R \left[\frac{3}{2} + \ln \left(\frac{\sqrt{\pi I_x I_y I_z}}{\sigma} \left(\frac{8\pi^2 k_B T}{h^2} \right)^{\frac{3}{2}} \right) \right] \text{ (for nonlinear molecules (H}_2\text{O))}$$

where m is the mass of the molecular system, R is the gas constant, P is the pressure, I_x , I_y , and I_z are the components of the inertia tensor along the principal directions, and I is the inertia moment for linear molecules.

The top and side views of DFT calculations for all the states are provided in Table S3.

Table S3. The top and side views of DFT calculations for all the states.

State	Top view	Side view
State1: $\text{H}_2^* + 2\text{O}^*$		
State2: TS1		
State3: $2\text{H}^* + 2\text{O}^*$		
State4: TS2		
State5: $\text{H}^* + \text{O}^* + \text{OH}^*$		
State6: TS3		
State7: $\text{O}^* + \text{H}_2\text{O}^*$		

References

- 1 J. Watt, C. Yu, S. L. Y. Chang, S. Cheong and R. D. Tilley, *J. Am. Chem. Soc.*, 2013, **135**, 606–609.
- 2 Z. You, K. Inazu, K. Aika and T. Baba, *Journal of Catalysis*, 2007, **251**, 321–331.
- 3 J. A. Mieth and J. A. Schwarz, *Journal of Catalysis*, 1989, **118**, 218–226.
- 4 B. Lin, R. Wang, J. Lin, S. Du, X. Yu and K. Wei, *Catalysis Communications*, 2007, **8**, 1838–1842.
- 5 Z. Akbari, M. D. Mensi, E. Oveisi, J. Ruffiner, W. Luo, C. D. Koolen and A. Züttel, *International Journal of Hydrogen Energy*, DOI:10.1016/j.ijhydene.2024.08.300.
- 6 I. Kennedy, H. Geering, M. Rose and A. Crossan, *Entropy*, 2019, **21**, 454.
- 7 E. Di Simone, G. Vilé, G. Di Liberto and G. Pacchioni, *ACS Catal.*, 2025, **15**, 447–456.
- 8 D. Carrasco-Busturia, *Journal of Physics and Chemistry of Solids*, 2021, **154**, 110045.